Chinese Chemical Letters 35 (2024) 109428

Contents lists available at ScienceDirect

Chinese Chemical Letters

journal homepage: www.elsevier.com/locate/cclet

Facile synthesis of porous TiO_2/SnO_2 nanocomposite as lithium ion battery anode with enhanced cycling stability *via* nanoconfinement effect

Xingang Kong[a,*], Yabei Su[a], Cuijuan Xing[b], Weijie Cheng[a], Jianfeng Huang[a], Lifeng Zhang[a], Haibo Ouyang[a], Qi Feng[a]

[a] *School of Materials Science and Engineering, Shaanxi University of Science and Technology, Xi'an 710021, China*
[b] *College of Chemistry and Chemical Engineering, Xingtai University, Xingtai 054001, China*

ARTICLE INFO

Article history:
Received 12 November 2023
Revised 6 December 2023
Accepted 19 December 2023
Available online 24 December 2023

Keywords:
Inverse opal TiO_2/SnO_2
Nanoconfinement
Lithium-ion batteries
Stability
Pseudocapacitance

ABSTRACT

SnO_2 is a potential anode material with high theoretical capacity for lithium-ion batteries (LIBs), however, its applications have been limited by the severe volume expansion during charging-discharging process. In this work, an inverse opal TiO_2/SnO_2 composite with an interconnect network nanostructure was designed to confine SnO_2 nanoparticles in the porous TiO_2. Due to this nanoconfinement structure, the volume expansion in the process was effectively alleviated, therefore the safety performance and cycling stability of the battery were effectively improved. At the same time, with a large number of microporous structures in the framework, the appearance of pseudocapacitance improves the rate performance and reversible capacity. In terms of electrochemical kinetics, its framework provides the connected path for charge migration, effectively reducing the charge transfer impedance, meanwhile, quantities of micropores in its skeleton could provide a smoother channel for lithium ions, thus greatly improving the diffusion rate of LIBs. The design of this nanostructure provides a new idea for the research of SnO_2-based anode with effectively enhanced electrochemical performance, which is promising anode for practical application.

The three-dimensional porous structure of inverse opal TiO_2/SnO_2 not only achieves excellent Li^+ storage mechanism by introducing pseudocapacitance, but also enhances its electrochemical kinetics *via* providing many fast channels for Li^+ and e^-.

Since SONY released the first commercial lithium-ion battery in 1990 [1], lithium-ion batteries (LIBs) have developed rapidly and are widely used in people's daily life including mobile phones, laptops, electric cars and aerospace [2–4]. Traditional LIBs usually use graphite materials as the anode electrode due to their low cost, environmental friendliness, and good electrical conductivity [5,6]. However, the theoretical capacity of graphite anode materials are only 370 mAh/g and there are safety problems such as the generation of lithium dendrites due to its low working potential (≈ 0 V *vs.* Li/Li^+) [7–9]. With the continuous increase of people's demand for electricity and the vigorous development of pure electric vehicles, graphite anodes gradually fail to meet the demand of high energy density, high security, and high capacity [10,11]. Therefore, it is necessary to find an alternative anode.

SnO_2-based anode materials have attracted the attention of many researchers in recent years due to their extremely high theoretical capacity (790 mAh/g) [12–14]. Liu *et al.* [15] prepared SnO_2 hollow spheres by self-assembled from nanosheets, which showed a reversible capacity of 607.2 mAh/g. Xu *et al.* [16] prepared uniform SnO_2 nanotubes with a mesoporous shell by a hard templates and it exhibited a reversible capacity of 513 mAh/g. However, the SnO_2-based anode materials have obvious volume expansion during charging and discharging process, which leads to pulverization of electrode material and short battery life, thus limiting its further application. To solve this problem, nanoconfinement treatment is an effective solution to significantly improve its cycling stability, capacity retention rate and cycling life [17–19].

Nanoconfinenment is achieved by encapsulating or limiting the nanospace in part or in whole. In addition, in the process of nanoconfined synthesis, the nanoconfined space can not only control the shape and size of the product, but also provide a specific environment for the nucleation, growth and stability of the product. Since nanopores are one of the most common nanoconfined

---

[*] Corresponding author.
E-mail address: yezhu_1983@163.com (X. Kong).

https://doi.org/10.1016/j.cclet.2023.109428

spaces, it is clear that the synthesis of porous structural materials such as graphene gels, organometallic frames, and porous organic polymers is a suitable method for creating nanoconfined spaces [20–22]. Ma *et al.* synthesized porous SnO_2/rGO xerogel as anode materials, which relieved the volume expansion of SnO_2 and increased the cycling stability [23].

TiO_2 has higher strength, negligible volume change and can provide a certain reversible capacity in the charging-discharging process, which is considered an ideal alternative material as the nanoconfinement materials [24–26]. In recent years, porous TiO_2 has been applied as framework materials for LIBs [27,28]. This special structure is interconnected, allowing electrons and ions to diffuse through adjacent pores, promoting electrolyte infiltration and improving electrical conductivity. For example, Liang *et al.* synthesized inverse opal $TiO_{2\text{-}X}$/Sulfur composite as Li-S cathode, which achieved long cycling life and high capacity [29]. Therefore, if it is used as the nanoconfinement material for SnO_2, not only the volume expansion problem can be effectively solved, but also the electrochemical kinetics of the electrode can be improved.

Herein, inverse opal TiO_2/SnO_2 (IO-TS) complex were synthesized as the LIBs anode. With the three-dimensional interconnected inverse opal TiO_2 as the nanoconfinement material, SnO_2 nanoparticles were successfully filled into its porous network. Due to this superior microstructure, the following enhanced electrochemical properties are achieved: (1) Its rate performance and cycling stability was effectively improved after TiO_2 nanoconfining treatment; (2) The volume expansion phenomenon of SnO_2 was obviously reduced during the charging-discharging process; (3) Due to its three-dimensional porous microstructure, pseudocapacitance was introduced, thus guaranteeing its reversible capacity to a certain extent; (4) In terms of electrochemical kinetics, its interconnected microstructure significantly reduces its charge transfer resistance and greatly increases the diffusion rate of LIBs. In this work, the TiO_2/SnO_2 composite showed enhanced electrochemical performance and provided a new research idea for the further popularization of SnO_2-based anode materials.

TiO_2 sol was obtained by sol-gel method mentioned in the literature [30]. Then the poly methyl methacrylate (PMMA was prepared according to the literature method, details are shown in Fig. S1 in Supporting information) was filtered to obtain the opal template, and the TiO_2 sol was filtered to make the TiO_2 fully filled. The above steps were repeated for many times, and then heat treated at 500 °C for 3 h to obtain inverse opal TiO_2, which was denoted as IO-TiO_2. Inverse opal TiO_2 was filtered with 5 mmol/L $SnCl_4$ ethanol solution, and then filtered with ammonia. The above steps were repeated for different times, and the obtained samples were recorded as IO-TS-1, IO-TS-2 and IO-TS-3, respectively. Finally, inverse opal TiO_2/SnO_2 was obtained by heat treatment at 500 °C for 3 h. By calculating the mass of samples before and after loading, the content of SnO_2 in IO-TS-2 is 23.57%, that in IO-TS-1 and IO-TS-3 are 9.42% and 37.14%. The concentration values C for electrodes determined are shown in Fig. S2 (Supporting information), respectively. The IO-TS preparation process is shown in Fig. 1. The details of characterization, preparation of the electrode, and electrical measurement are provided in Supporting information.

The crystal structures of IO-TiO_2, pure phase SnO_2 and IO-TS are shown in Fig. 2. It can be found that the XRD pattern of IO-TS shows the characteristic peaks of typical anatase TiO_2 (JCPDS card No. 21–1272) and rutile-type SnO_2 (JCPDS card No. 41–1445) [31,32]. All these three IO-TS samples show the phases of anatase TiO_2 and rutile-type SnO_2 without other impurity. The chemical composition and element chemical states of the composites were further confirmed by XPS (Figs. 2b–d). The high-resolution spectrum of Ti of IO-TS-2 presents two species: Ti $2p_{1/2}$ (464.3 eV) and Ti $2p_{3/2}$ (464.3 eV) which are in tune with anatase TiO_2. And the binding energy of Sn $3d_{5/2}$ (486.7 eV) and Sn $3d_{3/2}$ (495.3 eV) are in accordance with SnO_2. Moreover, O1s spectrum was deconvoluted into two peaks at 531.4 and 529.8 eV, belonging to chemisorbed oxygen crystal lattice oxygen, respectively (Fig. 2d) [33,34]. The overall XPS spectrum and high-resolution XPS spectra of the other two IO-TS samples for Ti, Sn and O elements are shown in Fig. S3 (Supporting information). All these results indicate that three IO-TS samples exhibit the phase of TiO_2/SnO_2 complex and are in good agreement with the XRD results.

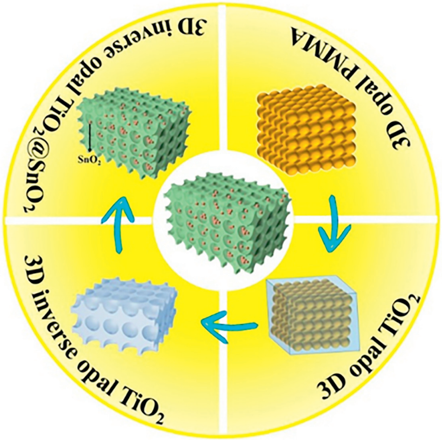

Fig. 1. Preparation process diagram of IO-TS composite material.

The SEM images of IO-TiO_2, SnO_2 and IO-TS-2 are displayed in Fig. 3. The initial morphologies of monodisperse colloidal microspheres PMMA are given in Fig. S4 (Supporting information). As shown in Fig. 3a, due to PMMA (Fig. S4) was used as the substrate, the obtained IO-TiO_2 has an ordered interconnected macropore structure, showing a three-dimensional porous framework connected by highly ordered nanoporous channels, which could provide many load sites for SnO_2. SnO_2 was used as the filler, and it has the morphology of nanoparticles with a particle size of about 150 nm (Fig. 3b). After the deposition of SnO_2, the SEM image of IO-TS-2 composite is presented in Fig. 3c, which maintains the same inverse opal structure as IO-TiO_2 while many SnO_2 particles are confined in the pores of TiO_2. Meanwhile, IO-TiO_2, IO-TS-1, IO-TS-2 and IO-TS-3 have large specific surface areas (Fig. S5 in Supporting information). This nanoscale hollow structure provides sufficient space for deposition of discharge products and volume expansion of SnO_2 during the cycling. At the same time, its three-dimensional interconnection network and the open channel could make the electrolyte easy to permeate and provide a faster transport path for LIBs. These properties of this structure may bring enhanced electrochemical performance for LIBs. And the SEM images of IO-TS-1 and IO-TS-3 are shown in Fig. S6 (Supporting information).

The TEM image of IO-TS is presented in Fig. 3d, and it displays the similar morphology with its SEM image. As shown in Fig. 3e, the lattice fringes with $d = 0.351$ nm can be attributed to (101) crystal planes of anatase TiO_2, aside from the lattice fringes of SnO_2 phase with $d_{(101)} = 0.264$ nm. The nanocomposite exhibits a polycrystalline SAED pattern, spotted diffraction rings confirmed the coexistence of polycrystalline TiO_2 and SnO_2, the d values of 0.243 nm and 0.318 nm correspond to the (103) plane of TiO_2 and (001) plane of SnO_2, respectively. More detailed TEM images of IO-TiO_2 are given in Fig. S7 (Supporting information). To determine the distribution of related element in IO-TS, the EDS test was carried out (Fig. S8 in Supporting information). The results showed that only Ti, O, Sn elements can be detected without other elements and these three elements were evenly distributed in the

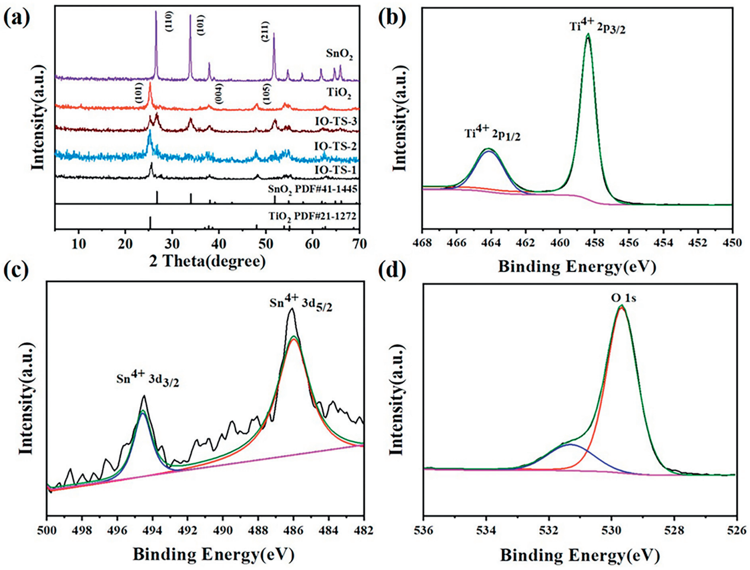

Fig. 2. XRD patterns of (a) IO-TiO$_2$, SnO$_2$, IO-TS-1, IO-TS-2 and IO-TS-3. The corresponding high-resolution XPS spectra of (b) Ti 2p, (c) Sn 3d and (d) O 1s of IO-TS-2.

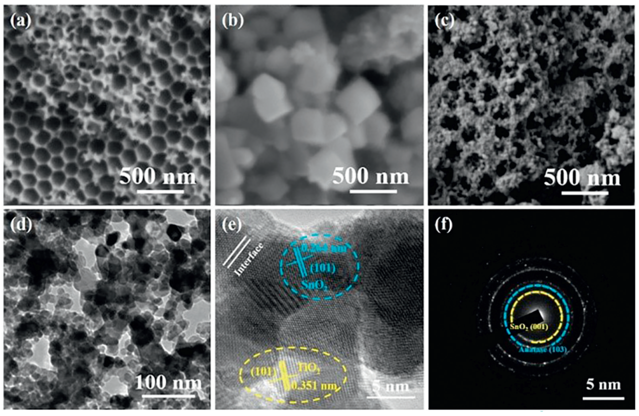

Fig. 3. SEM images of (a) IO-TiO$_2$, (b) SnO$_2$, (c) IO-TS-2, (d) TEM image, (e) HRTEM image and (f) SAED pattern of IO-TS-2.

material, indicating that the composition of the entire composite material is uniform.

The electrochemical performances of IO-TiO$_2$, IO-TS and SnO$_2$ are shown in Fig. 4. SnO$_2$ displays the higher capacity with poor rate performance while IO-TiO$_2$ exhibits lower capacity with excellent rate capability (Fig. 4a). When IO-TiO$_2$ was combined with SnO$_2$, the rate capability was enhanced. However, with the increase of the addition of SnO$_2$ contents, the capacity decreases, which is due to the higher SnO$_2$ contents block the porous structure IO-TiO$_2$, leading to the inefficient Li$^+$ transfer (Fig. 4a). Details of electrochemical performances for all samples can be seen in Table 1.

Cycling tests were performed on IO-TiO$_2$, IO-TS-2, and SnO$_2$ at a current density of 0.1 A/g, as shown in Fig. 4b. Inverse opal TiO$_2$ show discharge capacities of 568.3 mAh/g at the fist cycling, after 60 cycles, the specific capacity of IO-TiO$_2$ electrode is obviously rising because Li$^+$ storage is generated by pseudocapacitance during charge and discharge, thus increasing the specific capacity and energy density. After 100 cycles, the discharge capacity of IO-TiO$_2$ still remains 301.9 mAh/g which is higher than the most of other TiO$_2$-based anodes. As SnO$_2$ is an extremely high-capacity anode material (782 mAh/g), it shows a higher initial capacity of 800 mAh/g at fist cycling but its capacity decreases sharply to 200 mAh/g after 60 cycles, attributed to the serious volume expansion. After combined with IO-TiO$_2$, the cycling stability was improved due to the nanoconfinement effect of IO-TiO$_2$ and the synergistic effect [35] between IO-TiO$_2$ and SnO$_2$. The porous skeleton of IO-TiO$_2$ alleviates the volume expansion of SnO$_2$ during charge and discharge, and enhances the cycling stability. Meanwhile, The synergistic effect of polycrystalline TiO$_2$ and SnO$_2$ nanocomposites can decrease internal resistance which enhances the cycling stability of electrode. The IO-TS-2 showed the best cycling performance and high capacity among all the samples (Fig. 4b). After 100 cycles, IO-TS-2 can maintain a reversible capacity of 452 mAh/g, showing the highest capacity and cycling stability among all samples. As shown in Fig. S9 (Supporting information), since the SnO$_2$ content in

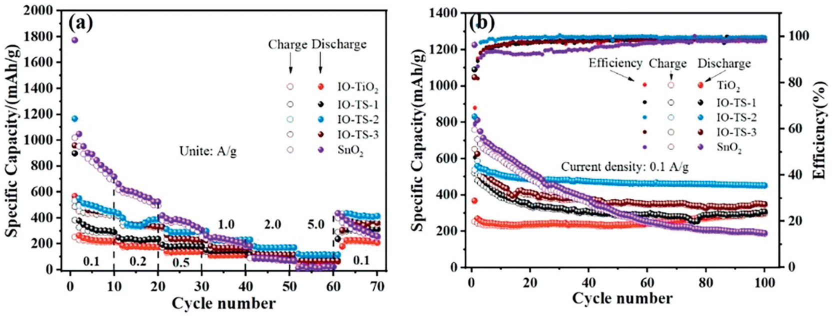

Fig. 4. The rate performances (a) of IO-TiO$_2$ IO-TS-1, IO-TS-2 and IO-TS-3 and SnO$_2$, cycling performances (b) of IO-TiO$_2$, IO-TS-1, IO-TS-2 IO-TS-3 and SnO$_2$ at 0.1 A/g.

Table 1
Charge and discharge capacities of four samples at each current density.

Material	Capacity (mAh/g)							
	Current density (A/g)	0.1	0.2	0.5	1.0	2.0	5.0	0.1
TiO_2	Discharge	223.2	175.7	141.2	114.5	89.5	62.6	209
	Charge	214.7	173.5	139.4	113.3	89.5	63.9	208.9
IO-TS-1	Discharge	289.7	237.5	181.1	143.7	105.1	78	316.2
	Charge	278	233.2	179.8	142.9	104.9	78.2	308.6
IO-TS-2	Discharge	447.3	389.2	297.5	232.4	172.2	115.3	415.5
	Charge	431.4	381	293.2	229.3	169.4	115.3	397.6
IO-TS-3	Discharge	435.3	332.9	229.6	167.5	115.3	69.4	362.1
	Charge	418.4	325	226.5	166.4	114.8	70.8	351.5
SnO_2	Discharge	709	525.1	305.6	189.5	72.1	20.8	258.5
	Charge	689.7	495.6	255.1	181.5	68.5	22.2	250.6

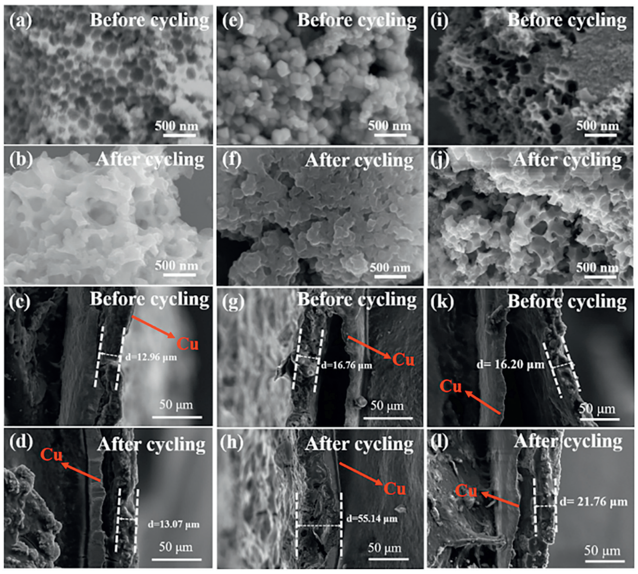

Fig. 5. The microtopography photographs of IO-TiO_2, SnO_2 and IO-TS-2 electrodes (a, e and i) before and (b, f and j) after cycling. The cross sections of the IO-TiO_2, SnO_2 and IO-TS-2 electrodes (c, g and k) before and (d, h and l) after cycling.

IO-TS-1 is lower, the particle size is smaller and most of SnO_2 fall on the framework of IO-TiO_2, so it is easier to fall off IO-TiO_2 skeleton during the cycling, resulting in capacity zttenuation during charge and discharge. The reason why the electrochemical stability of IO-TS-2 is higher than that of IO-TS-3 may be due to the excessive filling of SnO_2 hinder the Li^+ diffusion of in the porous framework and it will also take up too much vacant space, resulting in the inefficient diffusion during cycling.

To verify the excellent electrochemical stability of IO-TiO_2, IO-TS-2, and SnO_2 as anode materials for lithium-ion batteries, 100 charge/discharge tests were conducted. SEM photos of three sample electrodes after 100 times of charging and discharging are shown in Fig. 5. After 100 lithium and de-lithium cycles, IO-TiO_2 (Figs. 5a and b) and IO-TS-3 (Figs. 5e and f) electrodes still maintain the porous skeleton structure, which proves that IO-TiO_2 and IO-TS-3 have good cyclic stability and safety as the negative electrode of lithium ion batteries. SEM images before and after the cycling of SnO_2 (Figs. 5i and j) electrode showed that the morphology of SnO_2 electrode changed and the particles agglomerated during the process of lithium/de-lithium. By observing the cross sections of the electrodes before (Figs. 5g and k) and after (Figs. 5h and l) cycling, it can be found that the volume expansion rate of IO-TS-2 is 134%, which is lower than SnO_2 (328%). The electrode thickness almost did not change before and after IO-TiO_2 cycling (Figs. 5c and d). To probe the electrochemical behavior of IO-TS-2, the CV measurement was carried out in the potential range of 0.01–3.0 V at a scan rate of 0.1 mV/s (Fig. 6a). In the first cycling, the reduction peak of IO-TS is due to the formation of solid electrolyte interface (SEI) and the reduction of SnO_2 to metal Sn. The reduction peak at 1.1 V and the oxidation peak at 1.25 V is referenced to the partial reversible reaction described in Eq. 1 [36]. It can be seen from the second cycling, one pair of redox peaks at 1.7 V/2.17 V belongs to $Ti^{4+} \rightleftarrows Ti^{3+}$ of TiO_2 and the other two pair of peaks at 0.2 V/0.6 V [37,38] and 1.1 V/1.25 V correspond to the lithium/de-lithium of SnO_2 (Eq. 2 [36] and Eq. 3 [39]), respectively. The reduction and oxidation peaks of the last two cycling overlap very well, which means that after the first lithium reaction, the lithium/de-lithium reaction is highly reversible.

$$SnO_2 + 4Li^+ + 4e^- \rightarrow 2Li_2O + Sn \tag{1}$$

$$Sn + xLi + xe^- \leftrightarrow Li_XSn(0 \le X \le 4.4) \tag{2}$$

$$TiO_2 + xLi^+ + xe^- \leftrightarrow Li_xTiO_2(0 \le x \le 0.5) \tag{3}$$

Fig. 6b shows the charge-discharge voltage profiles of IO-TS-2 for the first 3 cycling at a current density of 100 mA/g with a voltage range of 0.01-3 V. The difference in discharge capacity between the first and last two turns can be attributed to the irreversible loss of Li^+ caused by the formation of SEI film corresponding well to CV result. It is obvious that IO-TS-2 exhibits a more retarded plateau below 1 V, due to that the addition of SnO_2 contributes to most of the capacity. At the same time, the discharge/charge curves of the second and third cycling are highly coincident, which also proved that IO-TS-2 has good cyclic stability.

Previous studies have shown that Li^+ storage is generated in the false capacitor during charging and discharging when porous materials are used as electrodes [40,41]. To verify whether there exists pseudocapacitance during charging and discharging, the volt-ampere cycling curve of IO-TS-2 at different scanning rates was measured (Fig. 6c) and the relationship between current and scanning speed was calculated. For a redox reaction, the peak current obey the power law [42]:

$$i = av^b \tag{4}$$

where i is the current (mA), v is the scanning rate (mV/s), a is an arbitrary coefficient, and b can be used as a factor to determine whether pseudocapacitor exists. The pseudocapacitance is obtained by calculating the function between the current and the scanning rate (Fig. 6d). The logarithm of both sides of the equation gives a linear relationship between log(i) and log(v), and the slope of this linear equation gives the value of b (Fig. 6d). According to the theory, if $b = 0.5$, it means that battery type Li^+ embedding (intercalation reaction) has occurred; if $b = 1$, it means that pseudocapacitive Li^+ storage has occurred. After fitting calculation, the b values of IO-TS-2 at the two lithiation peaks are 0.56 and 0.69, respectively. In other words, storage mechanisms represent a mixture of limited diffusion and capacity processes. This process is thought to increase the fluidity of materials.

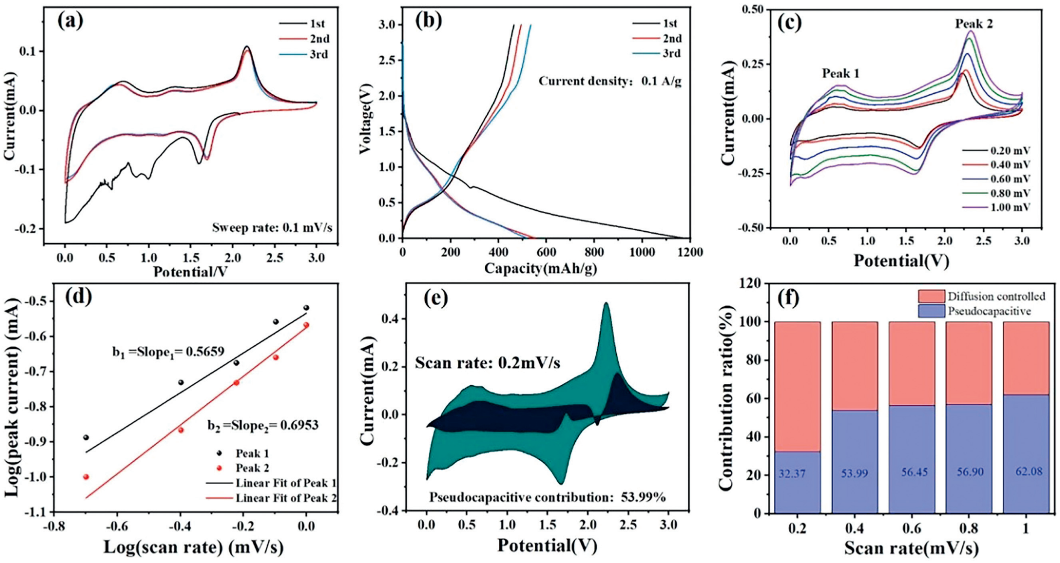

Fig. 6. (a) Volt-ampere cycling curves and (b) the capacity voltage curves of IO-TS-2. (c) Cyclic voltammetry test of IO-TS-2 at different sweep speed and (d) corresponding peak current versus square root of scan rates. (e) Pseudocapacitance contribution of IO-TS-2 at 0.2 mV/s. (f) Histogram of pseudocapacitance contribution at different scan rates.

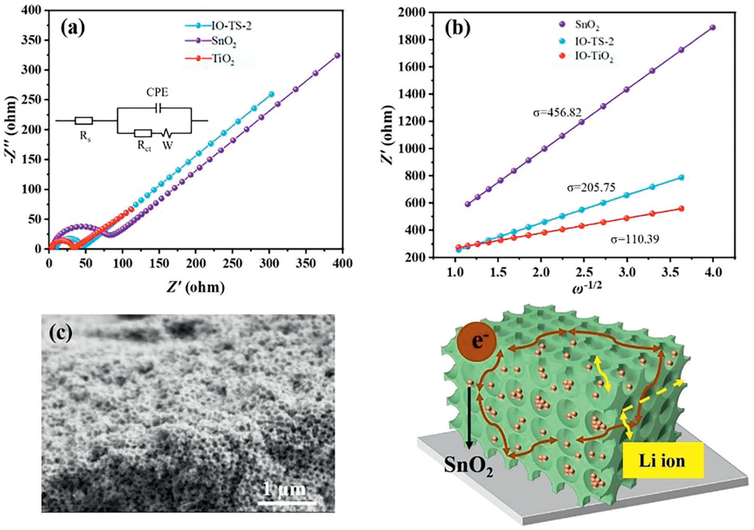

Fig. 7. (a) EIS measurements after cycling of IO-TiO$_2$, IO-TS-2 and SnO$_2$. (b) The slope of the plots of Z' against $\omega^{-1/2}$ of IO-TiO$_2$, IO-TS-2 and SnO$_2$. (c) Schematic diagram of fast charge transfer and Li$^+$ diffusion.

Furthermore, we calculated the ratio of pseudocapacitance of IO-TS-2 according to Eq. 5 [43]:

$$i(\mathrm{V}) = k_1 v + k_2 v^{1/2} \tag{5}$$

$k_1 v$ and $k_2 v^{1/2}$ respectively correspond to the current contribution of pseudocapacity and nested processes. Figs. 6e and f show the pseudocapacity ratio at 0.2 mV/s and the pseudocapacity ratio by running speed. Pseudocapacitance brings a huge capacity contribution at all scan rates, and the ratio of pseudocapacitance at the sweep speed of 0.2, 0.4, 0.6, 0.8 and 1.0 mV/s can reach 32.37%, 53.99%, 56.45%, 56.90% and 62.08% respectively (Fig. 6d). With it, as the scan rate increases, pseudocapacitance can occupy a leading position in the process, thereby storing Li$^+$. Pseudocapacity formed on the surface of the material cannot access the high current of the fast discharge process in such a short time.

EIS measurements were carried out to study the conductivity of the IO-TiO$_2$,IO-TS-2 and SnO$_2$ electrodes (Fig. 7). Samples of IO-TiO$_2$,IO-TS-2 and SnO$_2$ electrodes from 0.01 Hz to 1000 kHz electrochemical impedance spectrum (EIS) measurements of around 100 cycles in the frequency range were performed (all data were adjusted in *ZView*). Fig. 7a is the adjusted Nyquist curve and the equivalent impedance circuit after 100 cycling of 0.1 A/g. Herein, R_s is the internal resistance of the battery and is determined by the resistance of the electrolyte inside the battery, diaphragm and contact resistance of the battery shell; R_{ct} represents the charge transfer resistance, and it depends on how fast the charge travels [44]; In addition, the diagonal line represents the Wabur resistance (W) and the rate of diffusion of lithium ions in a battery system. The diffusion coefficient of lithium ions can be obtained by Eq. 6 [45].

$$D = \frac{R^2T^2}{2A^2n^4F^4C^2\sigma^2} \tag{6}$$

In formula R denotes a constant gas (8.314 J K^{-1} mol^{-1}) and T denotes the ambient temperature (298.15 K), A denotes the surface of the electrode (0.785 cm^2), and n denotes the number of electrons in the electronic transfer reactions. In respect of The Faraday constant (96,486 C/mol) is F, σ [46] is the slope of Z' and respect to $\omega^{1/2}$ (Fig. 7b), and C is the concentration of lithium-ion phase (mol/cm^3). In this study, the C value for IO-TiO$_2$,IO-TS-2 and

SnO_2 are 7.44×10^{-2}, 6.01×10^{-2} and 1.63×10^{-2} mol/cm^3, respectively. Table S1 (Supporting information) details the impedance of each component before and after the cycling and the three sample lithium-ion diffusion systems. The results show that the IO-TS-2 has lower charge-transfer resistance and a higher Li^+ diffusion coefficient. These performance improvements can be attributed to its special porous framework (Fig. 7c). Porous framework prevents the accumulation of particles to some extent, flattening the electron path and suppressing the resistance of charge movement. Small holes on the surface also provide Li^+ with many fast channels, which can increase Li^+ diffusion to some extent. Based on the above results, the excellent electrochemical properties were illustrated and demonstrated detailly in IO-TS.

In summary, the inverse opal TiO_2/SnO_2 composite were successfully prepared by mixing TiO_2 with $SnCl_4$ and then further treating it in air. In this rational design, the tin compound is effectively confined to a closed titanium dioxide frame due to physical capture and surface chemisorption. Inverse opal TiO_2 has good electrical conductivity and the advantages of small size nanopores, large specific surface area and high active material utilization. The hollow structure provides enough space to accommodate the volume expansion during cycling, achieving long cycling life and high capacity as anode in LIBs. Therefore, the inverse opal TiO_2/SnO_2 has the potential to be used as a new click structure for LIBs, which opens a new way to prepare tin-based electrode materials from metal oxides.

Declaration of competing interest

The authors declare that they have no known competing financial interests or personal relationships that could have appeared to influence the work reported in this paper.

Acknowledgments

The authors appreciate the support of Project Supported by Keypoint Research and Invention in Shaanxi Province of China (No. 2020GY-270), this work was supported by the National Natural Science Foundation of China (No. U22A20144).

References

[1] G. Kucinskis, G. Bajars, J. Kleperis, J. Power Sources 240 (2013) 66–79.
[2] N. Nitta, F.X. Wu, J.T. Lee, G. Yushin, Mater. Today 18 (2015) 252–264.
[3] M. Yilmaz, P.T. Krein, IEEE Trans. Power Electron. 28 (2013) 2151–2169.
[4] Z.H. Rao, S.F. Wang, Renew. Sustain. Energy Rev. 15 (2011) 4554–4571.
[5] L. Zou, F.Y. Kang, X.H. Li, et al., J. Phys. Chem. Solids 69 (2008) 1265–1271.
[6] J.X. Zhang, Z.W. Xie, W. Li, S.Q. Dong, M.Z. Qu, Carbon 74 (2014) 153–162.
[7] C. Shen, G.H. Hu, L.Z. Cheong, et al., Small Methods 2 (2018) 1700298–1700306.
[8] C.C. Chen, Y.A. Huang, C.H. An, et al., ChemSusChem 8 (2015) 114–122.
[9] X. Kong, J. Zhang, J. Huang, et al., Chin. Chem. Lett. 30 (2019) 771–774.
[10] H.L. Yu, J.N. Zhao, L.B. Ben, et al., ACS Energy Lett. 2 (2017) 1296–1302.
[11] M. Zier, F. Scheiba, S. Oswald, et al., J. Power Sources 266 (2014) 198–207.
[12] M.S. Park, G.X. Wang, Y.M. Kang, et al., Angew. Chem. Int. Ed. 46 (2007) 750–753.
[13] S.Z. Liu, K.L. Zhu, J.H. Tian, et al., J. Alloy Compd. 639 (2015) 60–67.
[14] Z.L. Yang, S.P. Zhao, W. Jiang, et al., Electrochim. Acta 158 (2015) 321–326.
[15] Q.N. Liu, Y.H. Dou, B.Y. Ruan, et al., Chem. Eur. J. 22 (2016) 5853–5857.
[16] X. Xu, J. Liang, H. Zhou, et al., J. Mater. Chem. A 1 (2013) 2995–2998.
[17] H.B. Li, J.P. Xiao, Q. Fu, X.H. Bao, Proc. Natl. Acad. Sci. U. S. A. 114 (2017) 5930–5934.
[18] X.L. Wang, G.S. Shi, S.S. Liang, et al., Phys. Rev. Lett. 121 (2018) 226102–2261027.
[19] S. Zhang, T. Hedtke, X. Zhou, M. Elimelech, J.H. Kim, ACS EST Eng. 1 (2021) 706–724.
[20] J. Ma, Y.R. Sun, M.Z. Zhang, et al., Environ. Sci. Technol. 51 (2017) 12283–12292.
[21] X.L. Zhang, J.L. Shen, S.Y. Pan, J.S. Qian, B.C. Pan, Adv. Funct. Mater. 30 (2020) 1909014–1909020.
[22] T.K. Vo, D.C. Hau, V.C. Nguyen, D.T. Quang, J. Kim, Appl. Surf. Sci. 546 (2021) 149087–149095.
[23] C. Ma, J.L. Jiang, T.T. Xu, et al., ChemElectroChem 5 (2018) 2387–2394.
[24] L. Sun, Z.L. Zhao, Y.C. Zhou, L. Liu, Nanoscale 4 (2012) 613–620.
[25] M.L. Lee, C.Y. Su, Y.H. Lin, et al., J. Power Sources 244 (2013) 410–416.
[26] J.F. Ye, W. Liu, J.G. Cai, et al., J. Am. Chem. Soc. 133 (2011) 933–940.
[27] H.W. Chen, Y.D. Lu, H.J. Zhu, et al., Electrochim. Acta 310 (2019) 203–212.
[28] H.G. Zhang, X.D. Yu, P.V. Braun, Nat. Nanotechnol. 6 (2011) 277–281.
[29] Z. Liang, G. Zheng, W. Li, et al., ACS Nano 8 (2014) 5249–5256.
[30] J.N. Gao, B. Jiang, C.C. Ni, et al., Appl. Catal. B: Environ. 254 (2019) 391–402.
[31] V. Perumal, C. Inmozhi, R. Uthrakumar, et al., Environ. Res. 209 (2022) 112821–112830.
[32] Y. Liu, Y. Jiao, Z. Zhang, et al., ACS Appl. Mater. Interfaces 6 (2014) 2174–2184.
[33] W.J. Cheng, Q. Feng, Z.L. Guo, et al., Chin. Chem. Lett. 33 (2022) 4776–4780.
[34] X. Shi, S.T. Liu, B. Tang, et al., Chem. Eng. J. 330 (2017) 453–461.
[35] X. Wang, W. Cheng, J. Hu, et al., Nanoscale 14 (2022) 13696–13710.
[36] R.Q. Liu, D.Y. Li, C. Wang, et al., Nano Energy 6 (2014) 73–81.
[37] W. Jiang, D. Xiong, S. Wu, et al., Ceram. Int. 48 (2022) 27174–27181.
[38] B. Wei, S. Yan, D. Jia, et al., Inorg. Chem. Commun. 145 (2022) 2587–2594.
[39] Z.Q. Wang, X. Li, H. Xu, et al., J. Mater. Chem. A 2 (2014) 12571–12575.
[40] F. Beguin, V. Presser, A. Balducci, E. Frackowiak, Adv. Mater. 26 (2014) 2219–2251.
[41] W.J. Cheng, Q. Feng, X. Wang, et al., Electrochim. Acta 440 (2023) 141758–141766.
[42] H. Lindström, S. Södergren, A. Solbrand, et al., J. Phys. Chem. B 101 (1997) 7717–7722.
[43] M. Lubke, P. Marchand, D.J.L. Brett, et al., J. Power Sources 305 (2016) 115–121.
[44] B.L. Corso, I. Perez, T. Sheps, et al., Nano Lett. 14 (2014) 1329–1336.
[45] C. Chen, C.C. Ai, Y.W. He, S. Yang, Y.X. Wu, J. Alloy Compd. 705 (2017) 438–444.
[46] X.Y. Du, W. He, X.D. Zhang, et al., J. Mater. Chem. 22 (2012) 5960–5969.